

## NATURAL HAZARDS

# Dual-initiation ruptures in the 2024 Noto earthquake encircling a fault asperity at a swarm edge

Liuwei Xu<sup>1</sup>, Chen Ji<sup>2\*</sup>, Lingsen Meng<sup>1\*</sup>, Jean-Paul Ampuero<sup>3</sup>, Zhang Yunjun<sup>4,5</sup>, Saeed Mohanna<sup>1</sup>, Yosuke Aoki<sup>6</sup>

To reveal the connections between the 2024 moment magnitude ( $M_w$ ) 7.5 Noto earthquake in Japan and the seismicity swarms that preceded it, we investigated its rupture process through near-source waveform analysis and source imaging techniques, combining seismic and geodetic datasets. We found notable complexity in the initial rupture stages. A strong fault asperity, which remained unbroken in preceding seismic swarms, slowed down the rupture. Then, a second rupture initiated at the opposite edge of the asperity, and the asperity succumbed to double-pincer rupture fronts. The failure of this high-stress drop asperity drove the earthquake into a large-scale event. Our observations help unravel the crucial role of fault asperities in controlling swarm migration and rupture propagation and underscore the need for detailed seismological and interdisciplinary studies to assess seismic risk in swarm-prone regions.

Large earthquakes, marked by powerful ground shaking and widespread damage, often involve multiple fault segments with intricate geometry and diverse physical properties [e.g., (1, 2)]. Even on a single fault, certain patches may exhibit higher shear stress or greater resistance to sliding owing to variations in loading rates, fault roughness, permeability, maturity, and other factors (3–5). Understanding the roles of fault heterogeneities in either impeding or facilitating earthquake rupture propagation is essential for seismic hazard assessment and mitigation. The 2024 moment magnitude ( $M_w$ ) 7.5 Noto earthquake and its preceding seismicity swarms, which occurred on the complex fault system beneath the Noto Peninsula, Japan, provide a valuable opportunity to explore these dynamics.

The earthquake occurred on 1 January 2024, originating on a reverse fault (Fig. 1) and resulting in a 4-m ground uplift along the peninsula's west coast and a 1.2-m tsunami (6). The faults beneath the Noto Peninsula were formed during the Japan Sea opening at the Oligocene period (~30 million years ago) (7) and had been hosting intense earthquake swarms since late 2020 (8–11). In 2023, the swarm turned into an earthquake sequence beneath the northeastern tip of the Noto Peninsula, featuring a  $M_w$  6.2 event and its largest  $M_w$  5.7 aftershock occurred within 2 months (9, 11, 12). Three independent geophysical observations

were reported: upward migration of small earthquakes [e.g., (12)], transient inflation with horizontal displacement of up to 30 mm and uplift of 70 mm at nearby geodetic stations (13), and a low  $S$ -wave velocity anomaly in the lower crust beneath these earthquakes (10). The seismic swarm has been attributed to the upward migration of fluids from the lower crust along a complicated fault system (8, 9, 11, 13). However, the role of the preceding seismic swarms in prompting the 2024 mainshock remains unexplained.

The 2024 Noto earthquake was well recorded by seismic and geodetic networks at local and teleseismic distances, allowing for in-depth analysis. We investigated the earthquake rupture process by using the slowness-enhanced back-projection (SEBP) (14, 15) and finite fault inversion (FFI) (16, 17) methods to analyze the global and local seismic data, as well as static surface deformation data obtained from global navigation satellite system (GNSS) stations and synthetic-aperture radar (SAR) satellites. We also examined seismic recordings from six nearby stations to unravel the earthquake's intricate early-stage rupture dynamics.

Our comprehensive approach provides a detailed characterization of the complex rupture process of the 2024 Noto earthquake. The mainshock has two distinct rupture initiations separated by ~10 s in time and 16 km in space. These dual initiations resulted in a double-pincer rupture propagation surrounding a strong fault asperity to the southwest of the hypocenter, which had been inactive during the preceding swarms, ultimately breaking it. The broken asperity hosted a high slip amplitude and stress drop, which were responsible for the intense ground shaking experienced on the Noto Peninsula. The rupture extended bilaterally to the southwest and northeast, with the northeast branch transitioning between fault segments with distinct dipping directions

before stopping near the boundary between the Amur and Okhotsk plates.

## Rupture fault, slip model, and detailed rupture kinematics

The high-frequency radiators imaged by SEBP [Figs. 1 and 2, figs. S1 to S5, and movies S1 to S4; see also (18)] and the spatial distribution of aftershocks reported between 1 and 21 January 2024 [Japan Meteorological Agency (JMA) catalog; Figs. 1 and 3, A and B] indicate a bilateral rupture comprising a northeast branch and a southwest branch. The northeast branch extends for ~60 km (Fig. 2) and halts offshore at the boundary between the Amur and Okhotsk plates (Figs. 1 and 2). The northeast rupture propagated over two fault segments of distinct dipping directions (Fig. 3, A and B): first on a southeastward-dipping segment (cross sections DD' to EE') and then on a northwestward-dipping segment (cross sections HH' to II'). The southwest branch propagated for ~85 km on two fault segments dipping southeastward (Figs. 1 to 3).

Using the aftershock distribution, JMA hypocenter, and long-period moment tensor solution of the Global Centroid Moment Tensor project, we constructed a three-segment fault model. Fault segments 1 and 2 exhibit a northeast strike and dip to the southeast, whereas segment 3 strikes southwestward and dips northwestward (Fig. 4 and fig. S6). We used a nonlinear finite fault inversion algorithm to constrain the fault slip, rupture initiation time, and starting and ending times of an analytic slip rate function for every subfault by jointly inverting seismic and geodetic data (18). Our analysis revealed that the 2024 Noto earthquake had a very complicated rupture history that lasted ~50 s (Fig. 4) and released a total seismic moment of  $2.2 \times 10^{20}$  newton meters (N·m) ( $M_w$  7.5). We show the resulting distributions of slip and rupture initiation time in Fig. 4A and the moment rate function in Fig. 2B. The fault slip is heterogeneous, including multiple higher slip patches ("asperities"). The average slip (4 m) of all areas with well-constrained slip amplitude exceeds the values expected from empirical scaling laws for interplate dip-slip earthquakes (2 m) and intraplate earthquakes (3 m) (19, 20).

The rupture of the 2024 Noto earthquake initiated at a depth of 10 km (the yellow star in Figs. 4 and 5, G and H, referred to as Hypo-I; JMA) on a fault plane dipping 40° to the southeast, within the intense and prolonged seismic swarm that has occurred since 2020 (Fig. 4C). The initiation stage of this rupture was especially well constrained by the records of three strong motion stations within 10 km of its epicenter (Fig. 5). Figure 5, A, C, and E, shows the broadband vertical ground displacement seismograms of the three closest

<sup>1</sup>Department of Earth, Planetary, and Space Sciences, University of California, Los Angeles, Los Angeles, CA, USA.

<sup>2</sup>Department of Earth Science, University of California, Santa Barbara, Santa Barbara, CA, USA. <sup>3</sup>Université Côte d'Azur, IRD, CNRS, Observatoire de la Côte d'Azur, Geozaur, Valbonne, France. <sup>4</sup>National Key Laboratory of Microwave Imaging, Aerospace Information Research Institute, Chinese Academy of Sciences, Beijing, China. <sup>5</sup>School of Electronic, Electrical, and Communication Engineering, University of Chinese Academy of Sciences, Beijing, China. <sup>6</sup>Earthquake Research Institute, University of Tokyo, Tokyo, Japan.

\*Corresponding author. Email: ji@geol.ucsb.edu (C.J.); lsmeng@ucla.edu (L.M.)

stations (ISK001, ISK002, and ISKH01; Fig. 5G) that were obtained by doubly integrating ground accelerations (2I), which are sensitive to the slip on the fault patches beneath these stations (17). The red lines are synthetic seismograms that were predicted using the preferred model. The mainshock hypocenter (Hypo-I) was at the southwest edge of an asperity (hereafter referred to as A-I; Fig. 5G), but the initial rupture did not immediately break A-I. Instead, it propagated unilaterally southwest toward another larger asperity (A-II) located 7 to 8 km away (Fig. 5G, fig. S7, and movie S5). As a result, the vertical displacement at station ISK001, which is located on top of the northeast edge of A-II, was much larger than that at the other two close stations in the first 10 s (Fig. 5, A, C, and E). The asperity A-II apparently acted as a “barrier” for the rupture propagation. After the rupture reached the northeast edge of A-II at about 4 s, it slowed down rapidly (Fig. 5G). The rupture almost stopped at about 10 s (see the local minimum of the moment rate function in Fig. 2B and closely spaced rupture time contours in the middle of Fig. 5G). Then, a new rupture emerged at the southwest side of A-II, approximately 16 km southwest of Hypo-I and at a depth of ~7 km (around the purple star in Figs. 4, B and

C, and 5, G and H, and table S1). We refer to the initiation point of this second rupture as Hypo-II. The rupture then propagated bilaterally. To the northeast of Hypo-II, the asperity A-II was broken from both sides, which described a double-pincer rupture propagation from 10 to 16 s (blue and purple arrows in Fig. 5, G and H). The seismic moment release during this 6-s-long period was equivalent to a  $M_w$  6.8 earthquake. Asperity A-I finally started failing at approximately 16 s from its southwest side and broke for another 8 s. This rupture scenario explains the observations at station ISK001 and ISKH01 (Fig. 5, A to D). Note that the vertical ground motion at station ISK001 developed again at about 14 s, much earlier than that at station ISKH01 (~22 s), which was located on top of A-I with the smallest epicenter distance of 3.9 km. Rupture continued for another 20 s, with substantial slip around 20 to 40 km east of the hypocenter, where segments 1 and 3 intersect. To the southwest of Hypo-II, large slip concentrated from -60 to -40 km along the strike, where segments 1 and 2 intersect. To account for the uncertainty of segment 1's dip angle and its potential influence

on Hypo-II, we conducted additional FFI with segment 1's dip angle varying from 32° to 46°. Hypo-II appears in all resolved slip models (fig. S8), and its location and timing are robust across all models (table S1).

In the above FFI, the strong motion velocity seismograms are filtered to less than 0.3 Hz (18) because the uncertainty in three-dimensional Earth velocity structure impedes high-frequency waveforms from being deterministically modeled. We then analyzed the high-frequency waveforms at six stations (ISK001, ISK002, ISK003, ISKH01, ISKH02, and ISKH03; Fig. 5 and figs. S9 to S11) to verify the Hypo-II location and time resolved in FFI. After first bandpass filtering the waveforms to 0.2 to 5 Hz and then estimating the envelopes (Fig. 5, B, D, and F, and fig. S10, B, D, F, H, J, and L), two wave groups could be seen at four stations (ISK001, ISK002, ISK003, and ISKH01). Stations ISKH02 and ISKH03 were added after the preliminary study to provide better constraints to Hypo-II. We handpicked the onset of the second group (vertical purple solid lines in Fig. 5, B, D, and F, and fig. S10) at each envelope, and subsequently found that these onsets can be well explained

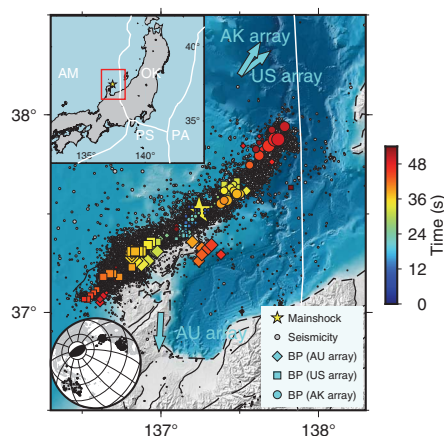


**Fig. 1. Tectonic map and summary of BP results.**

The colored symbols denote high-frequency radiators imaged by Australia (AU), US, and Alaska (AK) seismic arrays (see legend). The symbol size is proportional to the BP energy, and the color represents the rupture time with respect to the mainshock origin time. Cyan arrows indicate the azimuth toward each array. Gray dots denote the aftershocks that occurred from 1 to 21 January 2024, as reported by the JMA. The white line denotes the plate boundary between the Amur and Okhotsk plates (55). The upper inset shows the tectonic plate boundaries (white lines) and the source region shown in the main figure (red box). The lower inset shows the locations of the three seismic arrays. AM, Amur plate; OK, Okhotsk plate; PA, Pacific plate; PS, Philippine Sea plate.

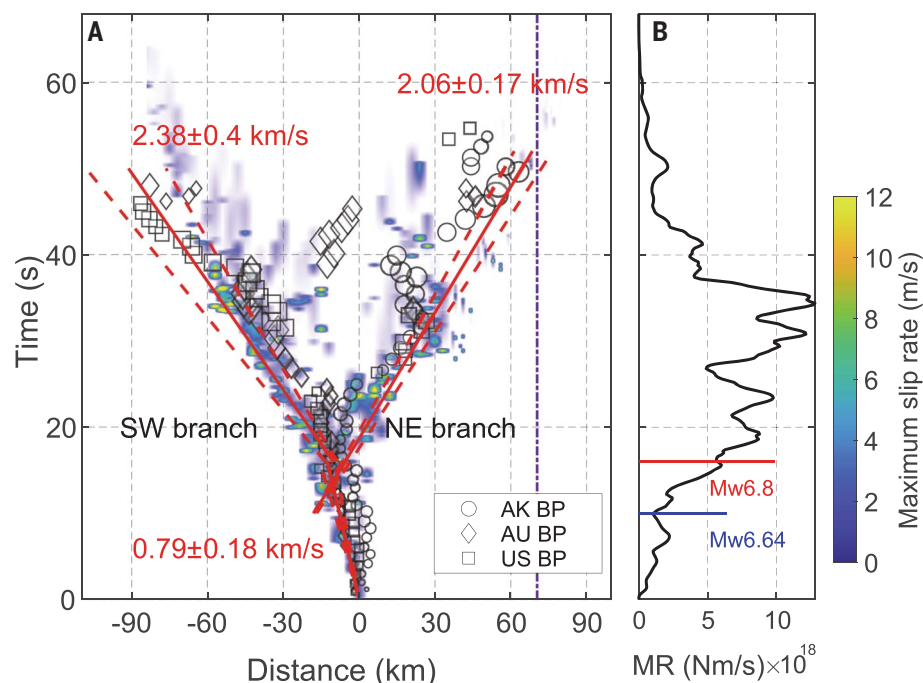


**Fig. 2. Rupture imaging and moment rate function.** (A) Constraints on rupture speeds from SEBP results (symbols) and comparison to FFI results (background colormap). Symbols indicate the location and timing of high-frequency radiators resolved by the Alaska array (white circles), the Australia array (white diamonds), and the US array (white squares). Location is defined as the along-fault position relative to the hypocenter, positive to the northeast (NE) and negative to the southwest (SW), accounting for the strike changes in the fault model of Fig. 4B. The red solid line shows the fitted steady rupture front, with average rupture speed indicated in red along with standard deviation (also shown by red dashed lines). The background colormap indicates the maximum slip rate among all depths from FFI. The vertical purple dashed line indicates the Okhotsk-Amur plate boundary's intersection with the FFI fault plane. (B) The moment rate (MR) function obtained by FFI. The blue and red labels indicate the equivalent magnitude of the seismic moment released, respectively, in the first 10 s and between 10 and 16 s.

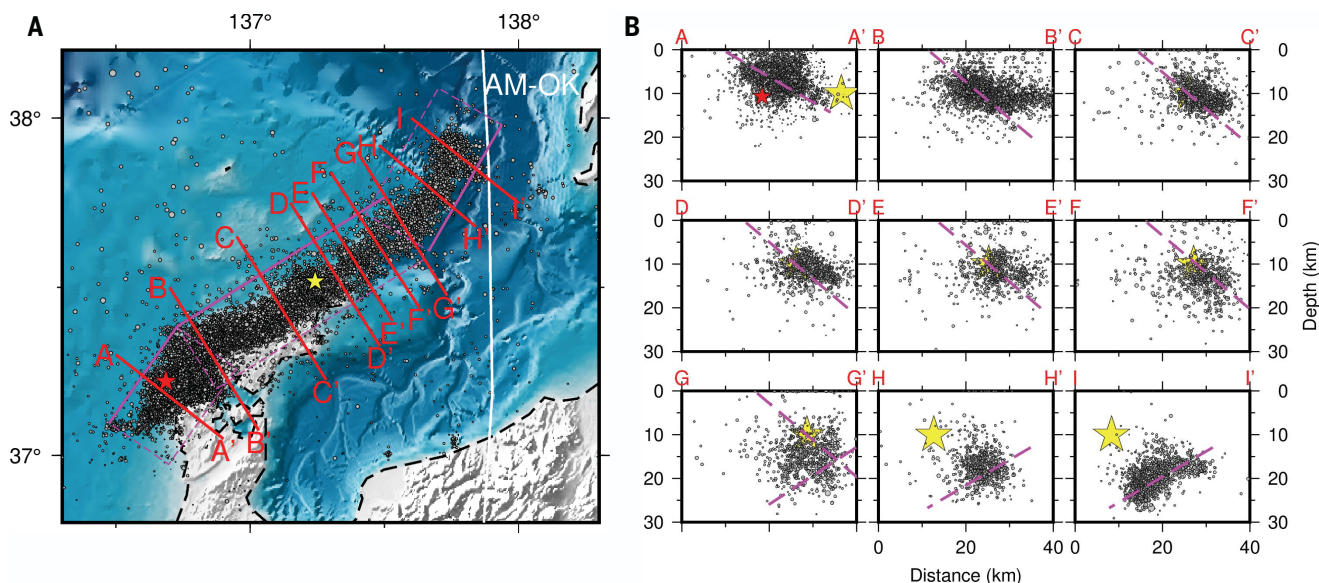


**Fig. 3. Aftershock distribution and fault geometry.** (A) Aftershocks that occurred from 1 to 21 January 2024, according to the JMA catalog (gray dots, with size proportional to magnitude). The yellow star denotes the epicenter of the 2024  $M_w$  7.5 event, and the red star denotes the epicenter of the 2007  $M_w$  6.6 event. The magenta boxes denote the fault planes adopted in our finite fault inversion, with the solid magenta lines indicating their upper boundaries. The

red lines indicate the cross sections shown in (B). The white line denotes the plate boundary between the Amur and Okhotsk plates (55). (B) Vertical cross-sectional views of seismicity along lines indicated in (A), within an 8-km distance to the lines. The magenta dashed lines in (B) denote the fault planes adopted in our finite fault inversion, and the magenta solid lines in (A) denote the upper boundary of the fault planes.

by  $S$  wave arrivals (vertical purple dashed lines in Fig. 5, B, D, and F, and figs. S10 and S11) from a point source at 10 s located at 137.07°E, 37.48°N, and 7 km depth (the purple star in Figs. 4, B and C, and 5, G and H) (18). Considering the uncertainties of both approaches, this location is nearly identical to the Hypo-II resolved by FFI (table S1).

The complex rupture evolutions were also resolved by SEBP (Fig. 2). The slow southwestward rupture was captured by SEBP results of the Australia array, with a propagation speed of 0.79 km/s (Fig. 2 and fig. S12). At approximately 10 s, FFI shows Hypo-II at approximately 16 km southwest of the first hypocenter. Subsequently, the southwest branch persisted for another ~33 s, extending to a distance of approximately ~85 km while the northeast branch also endured for a similar duration, reaching a distance of approximately 60 km. The average rupture speed of the northeast branch was 2.1 km/s, similar to the southwest speed of 2.4 km/s, considering the resolution and uncertainty of back-projection (BP). On segment 1 where the major coseismic slip occurred, BP radiators were primarily located at the down-dip edge of slip asperities (fig. S13). This distribution pattern is similar to what has been observed in some thrust earthquakes (22), where high-frequency radiators captured by teleseismic BP mainly image the deeper portions of the megathrust, and large fault displacements occur at shallower depths. The along-fault rupture speed and extent resolved by both methods are consistent (Fig. 2) (18), in-

dicating that coseismic slip and high-frequency radiators occur simultaneously at the same along-fault distance. The notable consistency between the two methods lends additional credibility to the accuracy of our rupture progression analysis.

#### Relation between earthquake initiation and growth and the preceding seismic swarm

The prolonged and intense earthquake swarm beneath the northeastern tip of the Noto Peninsula has been active since 2020 (9–11, 13). After the 2024  $M_w$  7.5 Noto earthquake, two crucial questions arose: Did the preceding seismic swarm prompt the occurrence of the 2024 mainshock, and why did the mainshock magnitude grow as large as 7.5?

To address the first question, we compared the swarm distribution with the mainshock hypocenter. A previous study (11) conducted a seismicity relocation analysis and found that seismic activity from 2020 to 2023 was organized into four clusters: south (cluster S), west (cluster W), north (cluster N), and east (cluster E). The swarm started in late 2020 at cluster S. About 5 months later, cluster W was activated (Fig. 4C) (11, 13). The swarm then migrated horizontally to clusters N and E (Fig. 4C) (11). Before the 2024 mainshock, most events of the swarm were small in magnitude, but collectively from November 2020 to December 2023, they cumulated a seismic moment of  $8.6 \times 10^{18}$  N·m [(11) and JMA catalog], equivalent to a  $M_w$  6.6 earthquake. The mainshock initiated within cluster N (Fig.

4C). The area near the mainshock hypocenter was seismically inactive until the seismic swarm migrated there in 2021. Within 3 km of the mainshock epicenter, 119 earthquakes of magnitude  $\geq 3$  occurred since 2021, including a magnitude 5.4 event in 2022 (11). By contrast, there was no earthquake of magnitude  $\geq 3$  from 2000 to 2020 [(11) and JMA catalog]. Thus, the preceding seismic swarm or its underlying driving process likely led to the nucleation of the 2024 Noto mainshock. The mainshock triggering could be the result of processes such as slow slip (23), fluid pressure perturbations (11), earthquake interactions by stress transfer (24), or a combination thereof.

The abnormal rupture history of asperity A-II helps address the second question. Decades of earthquake source studies revealed that fault stress and fracture energy (the energy dissipation needed to reactivate fault slip) distributions were often heterogeneous (3), resulting from nonuniform material distribution, previous deformation, and tectonic loading. Fault patches with higher shear-stress loading are usually named asperities, and those with higher fracture energy are barriers (3, 25). The failure of an asperity often leads to larger slip, whereas a barrier can slow down or even stop rupture propagation (3, 25). Before the breaking of A-II (in the initial 10 s), the northeastward rupture is weak and slow, and the southwestward rupture almost stops (Fig. 5G). The equivalent magnitude in the first 10 s is  $M_w$  6.64 (Fig. 2B). It is already a major event,

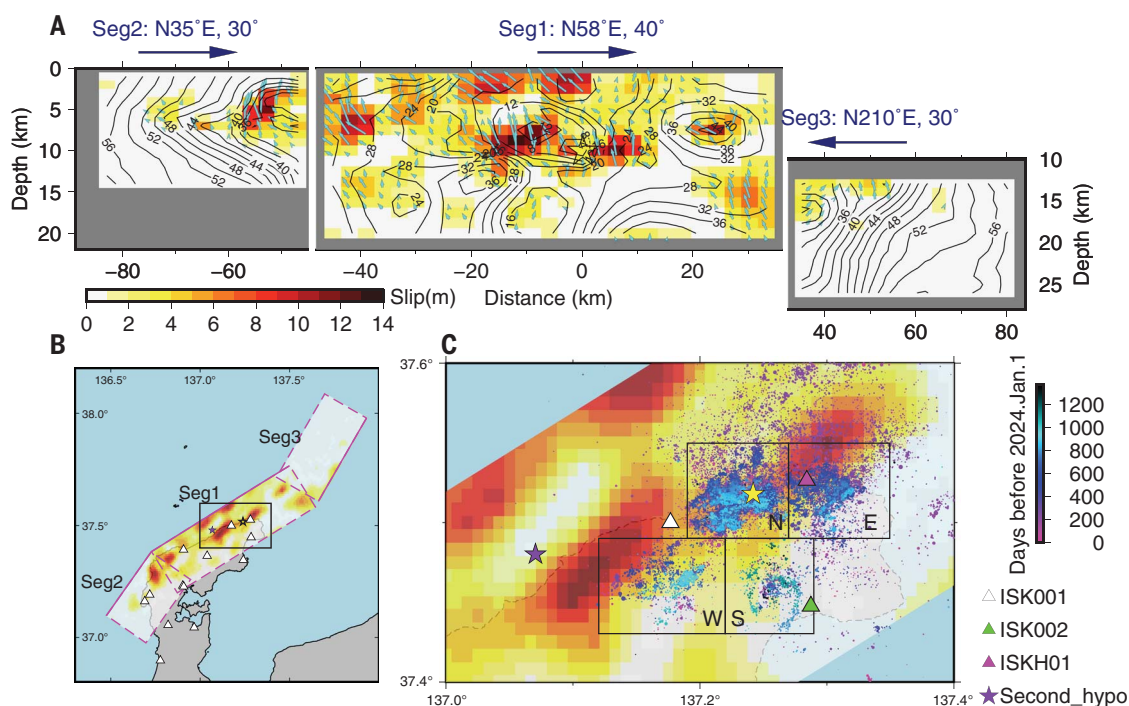


**Fig. 4. FFI results.** (A) Spatial distribution of final slip (colors), rupture initiation time (contours), and slip direction (rake angle, cyan arrows) along the fault system. Top labels indicate the orientation (strike angle) and dip angle of each fault segment.

(B) Map view of the slip and fault geometry model. The solid magenta lines denote upper boundaries of the fault planes. The box highlights the source region shown in (C). The white triangles denote strong motion stations adopted in the FFI (see fig. S9 for their names). The purple star denotes the second hypocenter, and the yellow star (outlined in black for visibility) denotes the first hypocenter.

(C) Seismicity [colored dots; (II) and JMA catalog]

occurring between January 2020 and 1 January 2024, color-coded by their time relative to the 2024 mainshock. The black boxes and labels indicate the south (S), west (W), north (N), and east (E) swarm clusters (II). Triangles denote the locations of three strong motion stations: ISK001, ISK002, and ISKH01 (see the legend on the right bottom).



but accounts for only 5.2% of the final seismic moment. After Hypo-II's initiation, the two rupture fronts associated with the two hypocenters encircle A-II and break it, generating substantial coseismic slip there. The average stress drop in A-II is ~40 MPa [fig. S14; see also (18)], which is substantially higher than the average asperity stress drop of crustal earthquakes in Japan (~10 MPa; (26)). The combination of high stress drop and large asperity size provides large potential energy to drive the rupture, resulting in a prolonged and extensive mainshock rupture (27, 28). Thus, asperity A-II acts as both a barrier and an asperity during this earthquake, and its failure is the reason why the 2024 Noto earthquake could develop into a  $M_w$  7.5 large-scale rupture. Interestingly, we observed a lack of swarm seismicity before 2024 within A-II, indicating that its behavior as a fault barrier was already apparent during the preceding swarm.

#### Implications for seismic hazard assessment

The spatial and temporal relationship between the preceding swarm from 2020 to 2023 and the subsequent devastating mainshock in 2024 beneath Noto Peninsula holds important implications for seismic hazard assessment. Before the mainshock, the long-term fault weakening process was evidenced by swarm migration (9, II). Notably, the fault patch A-II that was devoid of swarms was found to host substantial coseismic slip and stress drop during the

mainshock, leading to its escalation into a  $M_w$  7.5 event. This collective insight elucidates how seismic swarms, prestress, fault heterogeneities, and rupture dynamic interaction contribute to the development of large earthquakes. Regions that experience intense swarms thus warrant comprehensive studies that integrate both structural and source seismology, as well as other interdisciplinary approaches. For example, one important rock environment that hosts swarms, the fluid-filled porous fault, can be identified through magnetotelluric (29) and seismic tomography investigations (10). The swarm migration paths can be monitored by high-resolution seismicity location studies (9–II, 30). Our analysis further suggests that seismically quiescent fault areas in the vicinity of swarms could be the gate to future large earthquake ruptures and should be a particular focus of study. It also highlights that studies of earthquake predictability need to address the conditions not only for rupture initiation but also for rupture propagation and arrest.

It is worth noting that fault asperities and swarms do not invariably lead to major earthquakes. For instance, near Cahuilla, California, a prolonged and vigorous swarm from 2016 to 2019 exhibited a clear migration pattern (30). A low permeability fault zone at shallow depth initially limited the up-dip swarm migration, which was eventually circumvented but did not break. Laboratory experiments and numerical simulations have suggested

that factors such as asperity locations (31), ratio of the initial shear stress to the fault strength (32), normal stress level, fault roughness, and slip distance in the early rupture stage (33, 34) play crucial roles in determining whether an asperity will be seismically triggered. Detailed comparisons of fault properties, stress conditions, and background tectonics at natural earthquake scales could help decipher the differences that lead to varying outcomes. Furthermore, the fault responsible for the Noto earthquake presents a valuable case study for investigating changes in fault structure and stress after the mainshock, which can aid in assessing future seismic risks on the Noto Peninsula.

The present-day strain rate on the Noto Peninsula is low (35). Our model reveals up to 4 m of ground uplift near the west coast of the Noto Peninsula and ~2 m of uplift above A-II, which is greater than that observed in any documented historical earthquakes on the peninsula (e.g., the 1729 magnitude 6.6 event and the 2007  $M_w$  6.6 event) (36–38). Given the low long-term uplift rate estimated by geomorphological and geological studies (~1 mm/year) (39, 40), the substantial coseismic uplift indicates that if a  $M_w$  7.5 or similar magnitude event ever occurred and if the northern coastal uplift is attributed to repeated failures of A-II, such an earthquake might happen every few thousand years. Further research into topographic evolution and historical seismic activity is essential for identifying the recent events that

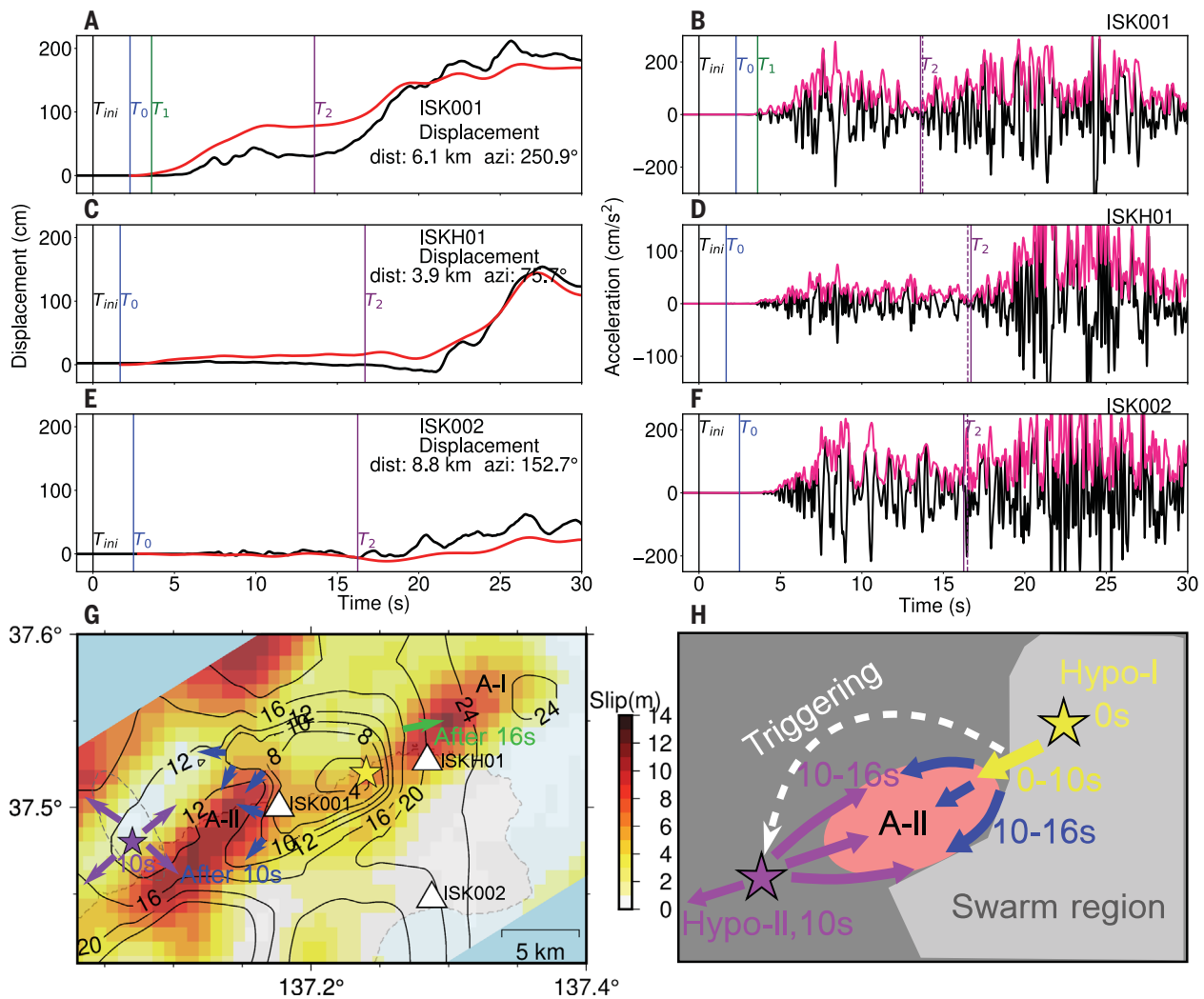


**Fig. 5. Dual-rupture initiations analysis.** (A) Vertical displacement (black line) obtained by integrating acceleration recording and removing the drift (2I) at station ISK001. The red line denotes the predicted waveform by the preferred FFI model.  $T_{ini}$  is the earthquake starting time (2024-01-01T07:10:08.33 UTC, JMA).  $T_0$  is the manually picked P wave arrival, based on (B).  $T_1$  is the manually picked beginning of the first wave group, based on (B).  $T_2$  with the solid purple line is the manually picked S wave arrival in the second wave group. The relative distance and azimuth from the hypocenter to the station are noted on the right. (B) Vertical acceleration seismogram recorded at station ISK001, bandpass filtered to 0.2 to 5 Hz. The pink line denotes the envelope of the waveform. The dashed purple line is the predicted S wave arrival time based on the best-fit second hypocenter location. (C and D) The same as (A) and (B) but for station

ISKH01. (E and F) The same as (A) and (B) but for station ISK002. (G) Sketch of the early rupture stage. The yellow star denotes the hypocenter (Hypo-I), and the purple star denotes the second hypocenter (Hypo-II). The background colors indicate final slip from FFI. The black contours and numbers denote the rupture time in seconds from FFI. The gray dashed ellipse around Hypo-II indicates its location uncertainty, that is, the 95% confidence interval in  $\chi^2$  uncertainty evaluation (18, 56). The purple arrows indicate the rupture propagation from Hypo-II. The blue arrows indicate the southwest rupture from Hypo-I. The green arrow indicates the northeast rupture from Hypo-I. The locations of A-I and A-II are indicated in the figure. (H) A schematic of the dual initiations and the double-pincer process that breaks A-II. The light gray region denotes the swarm occurrence region before 2024.

produced similar uplift, which will improve the accuracy of recurrence interval estimates for large earthquakes on the Noto Peninsula.

#### REFERENCES AND NOTES

1. L. Meng *et al.*, *Science* **337**, 724–726 (2012).
2. L. Xu *et al.*, *Commun. Earth Environ.* **4**, 379 (2023).
3. K. Aki, *J. Geophys. Res.* **89**, 5867–5872 (1984).
4. E. E. Brodsky, J. D. Kirkpatrick, T. Candela, *Geology* **44**, 19–22 (2016).
5. O. Zielke, M. Galis, P. M. Mai, *Geophys. Res. Lett.* **44**, 777–783 (2017).
6. S. Toda, R. S. Stein, "Intense seismic swarm punctuated by a magnitude 7.5 Japan shock," *Tremblor*, 4 January 2024;
7. L. Jolivet, K. Tamaki, M. Fournier, *J. Geophys. Res.* **99**, 22237–22259 (1994).
8. Y. Amezawa, Y. Hiramatsu, A. Miyakawa, K. Imanishi, M. Otsubo, *Geophys. Res. Lett.* **50**, e2022GL102670 (2023).
9. A. Kato, *Geophys. Res. Lett.* **51**, e2023GL106444 (2024).
10. J. Nakajima, *Earth Planets Space* **74**, 160 (2022).
11. K. Yoshida *et al.*, *Geophys. Res. Lett.* **50**, e2023GL106023 (2023).
12. K. Yoshida *et al.*, *J. Geophys. Res. Solid Earth* **128**, e2022JB026047 (2023).
13. T. Nishimura, Y. Hiramatsu, Y. Ohta, *Sci. Rep.* **13**, 8381 (2023).
14. L. Meng, A. Zhang, Y. Yagi, *Geophys. Res. Lett.* **43**, 628–636 (2016).
15. A. Zhang, dissertation, University of California, 2019.
16. C. Ji, D. J. Wald, D. V. Helmberger, *Bull. Seismol. Soc. Am.* **92**, 1192–1207 (2002).
17. C. Ji, D. V. Helmberger, D. J. Wald, K.-F. Ma, *J. Geophys. Res.* **108**, 2412 (2003).
18. Materials and methods are available as supplementary materials.
19. G. P. Hayes, *Earth Planet. Sci. Lett.* **468**, 94–100 (2017).
20. M. Leonard, *Bull. Seismol. Soc. Am.* **100**, 1971–1988 (2010).
21. D. M. Boore, *Bull. Seismol. Soc. Am.* **91**, 1199–1211 (2001).
22. T. Lay *et al.*, *J. Geophys. Res.* **117**, B04311 (2012).
23. P. Danré, D. Garagash, L. De Barros, F. Cappa, J.-P. Ampuero, *J. Geophys. Res. Solid Earth* **129**, e2023JB027276 (2024).
24. W. L. Ellsworth, F. Bulut, *Nat. Geosci.* **11**, 531–535 (2018).

25. E. M. Dunham, P. Favreau, J. M. Carlson, *Science* **299**, 1557–1559 (2003).
26. K. Irikura, H. Miyake, *Pure Appl. Geophys.* **168**, 85–104 (2011).
27. H. Kanamori, E. E. Brodsky, *Rep. Prog. Phys.* **67**, 1429–1496 (2004).
28. J. Li, T. Kim, N. Lapusta, E. Biondi, Z. Zhan, *Nature* **620**, 800–806 (2023).
29. K. Umeda, K. Asamori, A. Makuuchi, K. Kobori, Y. Hama, *J. Geophys. Res. Solid Earth* **120**, 2279–2291 (2015).
30. Z. E. Ross, E. S. Cochran, D. T. Trugman, J. D. Smith, *Science* **368**, 1357–1361 (2020).
31. L. Wang, S. Xu, Y. Zhuo, P. Liu, S. Ma, *Earth Planet. Sci. Lett.* **636**, 118711 (2024).
32. S. Lee, E. Choi, C. H. Scholz, *J. Geophys. Res. Solid Earth* **128**, e2023JB027551 (2023).
33. P. A. Selvadurai, S. D. Glaser, *J. Geophys. Res. Solid Earth* **120**, 4208–4236 (2015).
34. P. A. Selvadurai, S. D. Glaser, *Geophys. J. Int.* **208**, 1009–1025 (2016).
35. T. Nishimura, Y. Yokota, K. Tadokoro, T. Ochi, *Geosphere* **14**, 535–551 (2018).
36. T. Usami, *Materials for Comprehensive List of Destructive Earthquakes in Japan [Latest Edition] [416]–2001* (Univ. Tokyo Press, 2003).
37. M. Hamada, Y. Hiramatsu, M. Oda, H. Yamaguchi, *Tectonophysics* **670**, 38–47 (2016).
38. S. Ozawa, H. Yari, M. Tobita, H. Une, T. Nishimura, *Earth Planets Space* **60**, 95–98 (2008).
39. Y. Ota, K. Hirakawa, *Geogr. Rev. Jpn.* **52**, 169–189 (1979).
40. M. Shishikura, T. Echigo, Y. Namegaya, *Active Fault Research* **2020**, 33–49 (2020).
41. P. A. Rosen, E. Gurrola, G. F. Sacco, H. Zebker, paper presented at EUSAR 2012, 23 to 26 April 2012, Nuremberg, Germany.
42. Z. Yunjun, yunjun/2024-Noto-EQ: Version 1.0 (v1.0). Zenodo (2024); <https://doi.org/10.5281/zenodo.12803386>.
43. L. Xu, L. Meng, Codes for slowness-enhanced back-projection (SEBP). Zenodo (2024); <https://doi.org/10.5281/zenodo.12801968>.
44. U.S. Geological Survey, Earthquake Hazards Program, Advanced National Seismic System (ANSS) Comprehensive Catalog of Earthquake Events and Products: Various (2017); <https://doi.org/10.5066/F7MS3QZH>.
45. A. M. Dziewonski, T.-A. Chou, J. H. Woodhouse, *J. Geophys. Res.* **86**, 2825–2852 (1981).
46. G. Ekström, M. Nettles, A. M. Dziewonski, *Phys. Earth Planet. Inter.* **200–201**, 1–9 (2012).
47. R. Newman *et al.*, Wilber 3: A Python-Django web application for acquiring large-scale event-oriented seismic data (Incorporated Research Institutions for Seismology, 2013); <https://ds.iris.edu/wilber3/>.
48. A. Strollo *et al.*, *Seismol. Res. Lett.* **92**, 1788–1795 (2021).
49. National Research Institute for Earth Science and Disaster Resilience, NIED K-NET, KiK-net, National Research Institute for Earth Science and Disaster Resilience. NIED Repository (2019); <https://doi.org/10.17598/NIED.0004>.
50. M. Beyreuther *et al.*, *Seismol. Res. Lett.* **81**, 530–533 (2010).
51. P. Wessel, W. H. F. Smith, *Eos* **79**, 579 (1998).
52. R. B. Lohman, W. D. Barnhart, *J. Geophys. Res. Solid Earth* **115**, 12413 (2010).
53. L. Xu, Z. Yunjun, The results and datasets of 2024 Mw 7.5 Noto earthquake. Zenodo (2024); <https://doi.org/10.5281/zenodo.12786109>.
54. P. Koch, F. Bravo, S. Riquelme, J. G. F. Crempien, *Seismol. Res. Lett.* **90**, 1971–1986 (2019).
55. P. Bird, *Geochim. Geophys. Geosyst.* **4**, 1027 (2003).
56. P. Shearer, *Introduction to Seismology* (Cambridge Univ. Press, ed. 2, 2009).

## ACKNOWLEDGMENTS

We thank J. Nakajima, K. Asano, and T. Iwata for sharing the velocity model of Noto Peninsula. We thank J. Nakajima, T. Nishimura, K. Yoshida, and the Japan Meteorological Agency (JMA) for sharing the seismicity catalogs; the Japan Aerospace Exploration Agency (JAXA) for sharing the ALOS-2 SAR data; and the Geospatial Information Authority of Japan (GSI) and Nevada Geodetic Laboratory for releasing the GNSS data. We thank P. Bird and C. Liang for fruitful discussions. We thank three anonymous reviewers for their constructive comments and suggestions.

**Funding:** This work was funded by a NSF CAREER grant, EAR-1848486 (L.X., L.M., and S.M.), the Leon and Joanne V.C. Knopoff Fund (L.M.), grants from the Southern California Earthquake Center (SCEC), funded by NSF cooperative agreement EAR-0109624 and US Geological Survey (USGS) cooperative agreement 02HQAG0008 (C.J.); and the UCA<sup>JEDI</sup> Investments in the Future project (ANR-15-IDEX-01) managed by the National Research Agency of the French government (J.-P.A.). **Author contributions:** Conceptualization: C.J., L.M., J.-P.A.; Methodology: L.X., C.J., L.M.,

Z.Y., Y.A.; Investigation: L.X., C.J., L.M., Z.Y., S.M.; Visualization: L.X., Z.Y.; Supervision: C.J., L.M., J.-P.A.; Writing—original draft: L.X., C.J., Z.Y., J.-P.A.; Writing—review and editing: L.X., C.J., L.M., J.-P.A., S.M., Z.Y., Y.A. **Competing interests:** The authors declare that they have no competing interests. **Data and materials availability:** All data are available in the main text or the supplementary materials. The SAR processing was performed using the ISCE-2 software, available at <https://github.com/isce-framework/isce2> (41), with the postprocessing recipe available at Zenodo (42). The MATLAB code of SEBP is available at Zenodo (43). The moment tensor solutions came from the USGS (<http://earthquake.usgs.gov>) (44) and the Global Centroid Moment Tensor project (<http://www.globalcmt.org>) (45, 46). All teleseismic data were downloaded through the IRIS Wilber 3 system (<https://ds.iris.edu/wilber3/>) (47) and ORFEUS ([www.orfeus-eu.org](http://www.orfeus-eu.org)) (48). The local strong motion data were downloaded from the National Research Institute for Earth Science and Disaster Resilience ([https://www.kyoshin.bosai.go.jp/kyoshin/quick/index\\_en.html](https://www.kyoshin.bosai.go.jp/kyoshin/quick/index_en.html)) (49). The Python software package Obspy ([www.obspy.org](http://www.obspy.org)) (50) was used for seismic data requesting and waveform filtering. Figures were produced using Generic Mapping Tools (GMT) (51). Obspy, and Matlab. The static displacement data were downsampled by InSamp (<https://github.com/williamBarnhart/InSamp>) (52). The SEBP results, the preferred slip model, the strong motion and GNSS station lists, and the SAR data used in the study are available at Zenodo (53). The finite fault inversion code is publicly available on Github repositories of the USGS at <https://code.usgs.gov/ghsc/neic/algorithms/neic-finitefault> (54). **License information:** Copyright © 2024 the authors, some rights reserved; exclusive licensee American Association for the Advancement of Science. No claim to original US government works. <https://www.science.org/about/science-licenses-journal-article-reuse>

## SUPPLEMENTARY MATERIALS

[science.org/doi/10.1126/science.adp0493](https://science.org/doi/10.1126/science.adp0493)  
Materials and Methods  
Figs. S1 to S26  
Tables S1 to S7  
References (57–69)  
Movies S1 to S5

Submitted 10 March 2024; accepted 23 July 2024  
10.1126/science.adp0493